QUARTERLY JOURNAL OF THE ROYAL METEOROLOGICAL SOCIETY
Q. J. R. Meteorol. Soc. **134**: 859–874 (2008)
Published online 3 June 2008 in Wiley InterScience
(www.interscience.wiley.com) DOI: 10.1002/qj.262

RMetS
ROYAL METEOROLOGICAL SOCIETY

The impact of deformation strain on the formation of banded clouds in idealized modelling experiments

S. L. Gray* and H. F. Dacre
Department of Meteorology, University of Reading, UK

ABSTRACT: Experiments are performed using an idealized version of an operational forecast model to determine the impact on banded frontal clouds of the strength of deformational forcing, low-level baroclinicity, and model representation of convection. Line convection is initiated along the front, and slantwise bands extend from the top of the line-convection elements into the cold air. This banding is attributed primarily to ΔM adjustment. The cross-frontal spreading of the cold pool generated by the line convection leads to further triggering of upright convection in the cold air that feeds into these slantwise bands. Secondary low-level bands form later in the simulations; these are attributed to the release of conditional symmetric instability. Enhanced deformation strain leads to earlier onset of convection and more coherent line convection. A stronger cold pool is generated, but its speed is reduced relative to that seen in experiments with weaker deformational strain, because of inhibition by the strain field. Enhanced low-level baroclinicity leads to the generation of more inertial instability by line convection (for a given capping height of convection), and consequently greater strength of the slantwise circulations formed by ΔM adjustment. These conclusions are based on experiments without a convective-parametrization scheme. Experiments using the standard or a modified scheme for this model demonstrate known problems with the use of this scheme at the awkward 4 km grid length used in these simulations. Copyright © 2008 Royal Meteorological Society

KEY WORDS conditional symmetric instability (CSI); ΔM adjustment; slantwise circulations

Received 30 March 2007; Revised 28 March 2008; Accepted 14 April 2008

1. Introduction

Both singly- and multiply-banded clouds are often observed in the frontal zones of baroclinic cyclones. A wide range of banding may occur, with band spacings varying from 20 km to 100 km (see, for example, Novak *et al.* (2004), and see Lagouvardos *et al.* (1993) for a review of observed cases). Radar observations have shown the coexistence of upright and slantwise convection in these bands (e.g. Browning *et al.*, 2001). Accurate forecasting of the spatial distribution of these bands is crucial for accurate flood forecasting (especially for catchments whose scale is similar to the band separations). However, these bands can be poorly resolved in operational mesoscale model forecasts, with typical horizontal grid spacings of around 10 km; Knight and Hobbs (1988) found that a grid spacing of 10 km or less was required to resolve slantwise banding, and Lean and Clark (2003) found that a grid spacing of 2 km in the horizontal and 90 vertical levels were required to represent small-scale multiple slantwise circulations similar to those observed in dropsonde data. The mechanisms leading to band formation, and the sensitivity of the formation and maintenance of these bands to factors such as the large-scale frontal forcing, the frontal strength (baroclinicity) and local convective instability are still relatively poorly understood, despite substantial published literature (see Schultz and Schumacher (1999) for a review). The goal of this study is to determine the dependence of banded clouds associated with multiple mesoscale circulations in frontal zones on large-scale deformation. We have systematically tested the dependence of banding on large-scale deformation strain using an idealized version of an operational forecast model. Use of this model was motivated by the need for our results to be directly relevant to operational forecasts.

Several mechanisms have been proposed for the formation of banded clouds; but such clouds are usually attributed to one of two mechanisms: a type of moist symmetric instability (MSI) termed 'conditional symmetric instability' (CSI); or a type of inertial instability termed 'ΔM adjustment'. CSI arises because of the gravitational and inertial instability of air parcels displaced along a slanted path under conditions where vertically-displaced parcels are gravitationally stable and horizontally-displaced parcels are inertially stable (Bennetts and Hoskins, 1979; Emanuel 1983). ΔM adjustment arises when upright convection in a baroclinic zone leads to mid-tropospheric subgeostrophic momentum anomalies that adjust inertially along slantwise paths (Holt and Thorpe, 1991; Fischer and Lalaurette, 1995b). The relative importance of these two mechanisms in frontal zones is not known (see Pizzamei *et al.* (2005) and Schultz

* Correspondence to: S. L. Gray, Department of Meteorology, University of Reading, PO Box 243, Reading, Berkshire, RG6 6BB, UK. E-mail: s.l.gray@rdg.ac.uk

and Schumacher (1999) for more details of these mechanisms). Xu and Clark (1985) and Xu (1986a) argue for the existence of a continuum between buoyancy and inertial and symmetric instabilities, with 'pure' buoyancy and inertial instabilities (those existing in the absence of basic-state shear) being limiting cases of symmetric instability. However, the distinction between these instabilities has been of interest to many authors, not least because of the different growth rates and orientations of the circulations resulting from their release.

Pizzamei *et al.* (2005) recently examined the interaction between upright and slantwise convection in a frontal zone using an idealized modelling environment (a two-dimensional cloud-resolving model). Convection was artificially triggered in the frontal zone. Further triggering was found to occur on both the warm and the cold side of the frontal zone, and was forced by a spreading cold pool arising from evaporation in the slantwise downdraught. The initially upright plumes became tilted, as ΔM adjustment led to multiply-banded clouds. Schultz (2006) argued that the lack of a large-scale deformation field (which could continuously trigger ascent) in these simulations was a critical omission, as large-scale forcing is necessary for frontogenesis. In response, Gray and Browning (2006) acknowledged the need to address this issue and referred to the research work presented in the present paper, which at the time was ongoing. The dependence of banding in frontal zones on the large-scale forcing is not known. Xu (1992) found (using a viscous semi-geostrophic model) that a deformation flow squeezes the multiple bands produced toward the front, and stretches them along it, leading to merging of the multiple bands into a single band. Fischer and Lalaurette (1995b) found (in two-dimensional primitive-equation model simulations of an observed case) that CSI is only released for small deformation forcing, since confluence rapidly shrinks the area fulfilling the criteria for CSI; they concluded that the release of CSI is 'not likely to occur in active fronts'. They also concluded that ΔM adjustment is more likely to occur in fronts than the release of pure modal CSI. These studies demonstrate the need to address this issue.

In this study, we use an idealized version of an operational (full-physics) forecast model, which has previously been used for frontal simulations with large-scale forcing (Forbes, 2002; Dacre and Gray, 2006). The use of an operational mesoscale model necessitates consideration of implementation issues associated with such models, particularly the representation of convection at high resolution. Convection in nature occurs on spatial scales similar to the grid spacings of current mesoscale models (4–30 km). In the absence of a clear separation of scale between the convective scales and grid scales (so that a grid box does not contain many convective clouds), the theory of parametrization breaks down, but parametrization is still necessary to remove instability on subgrid scales. This was recognized by Kuo *et al.* (1997) in a review of parametrization in mesoscale models. The behaviours of parametrized versus explicit treatments of convection are dependent on the large-scale environment and forcing (Done *et al.*, 2006). Hence, in this study we consider both parametrized and explicit representations of convection.

The objectives of this study are to:

- simulate banded frontal clouds in an idealized version of an operational forecast model;
- determine the mechanisms of interaction between upright and slantwise convection;
- determine the dependence of banded frontal clouds on the strength of deformational forcing, the low-level baroclinicity and the representation of convection (parametrized or explicitly resolved).

The model used, and its configuration, are described in Section 2. The details of the simulations performed and diagnostics used are described in Section 3. Results are presented in Section 4: starting with the evolution of the control simulation, followed by the dependence on large-scale deformation strain and low-level baroclinicity, and finishing with the dependence on the representation of convection in the model. Discussion and conclusions are given in Section 5.

2. Model and initialization

The model configuration closely follows that described in Dacre and Gray (2006), but with a thermodynamic profile based on an observed case.

2.1. Model description

The idealized version of the Met Office non-hydrostatic Unified Model (version 5.3) is used. This model solves non-hydrostatic deep-atmosphere dynamics using a semi-implicit semi-Lagrangian numerical scheme (Cullen *et al.*, 1997). The model includes a comprehensive set of parametrizations, including parametrizations for the boundary layer (Lock *et al.*, 2000), mixed-phase cloud microphysics (Wilson and Ballard, 1999), and convection (Gregory and Rowntree, 1990). The radiation scheme is excluded, as radiation is unlikely to be important on the time-scales relevant to this study (of the order of a day). Thus the idealized version of the model includes the same physics and dynamics as the operational forecast model but with an idealized setup. The model runs on a rotated latitude–longitude horizontal grid with Arakawa C staggering, and a terrain-following hybrid-height vertical coordinate with Charney–Philips staggering. The model is on an f-plane, with a Coriolis parameter appropriate for the latitude 55 °N ($f = 1.19 \times 10^{-4}$ s^{-1}). The domain is entirely over the sea, with a uniform sea-surface temperature of 11 °C. A domain with a horizontal grid spacing of 0.036° (approximately 4 km) is used, with 180×180 grid points in the horizontal. The vertical grid spacing increases with height from the surface to the top of the model at 16 km. The

DOI: 10.1002/qj

model is run with 64 vertical levels; this gives a grid spacing of 200–300 m in the mid-troposphere, with higher resolution near the surface in the boundary layer. This horizontal resolution is coarser than the optimal resolution for resolving small-scale multiple slantwise circulations (according to Lean and Clark (2003) and Morcrette and Browning (2006)), but was chosen to make these large-domain simulations manageable. Morcrette and Browning (2006) found that simulations with 4 km horizontal grid boxes produced circulations similar to those obtained with finer resolutions, although they took longer to evolve. Vertical resolution is also important. Persson and Warner (1993) found that a maximum horizontal grid spacing of 15 km, and a vertical grid spacing of 170 m, were necessary to resolve the most unstable linear CSI modes. They found that failure to resolve these modes leads to weaker circulations with a smaller growth rate. Lean and Clark (2003) note that they would expect the numerical dissipation associated with the least well-resolved direction (horizontal or vertical) to dominate the solution of the model integration for the Unified Model. For a 4 km grid spacing, the solutions are dominated to an equal degree by the vertical and horizontal resolutions for a vertical grid spacing of approximately 150 m in the mid-troposphere (90 model levels using their vertical grid).

2.2. Initial and boundary conditions

The initial thermodynamic profile is specified by defining temperature and relative humidity at a series of heights. It is idealized, but loosely based on the ana-cold-frontal case of 10 February 2000, in which two stacked slantwise layers were observed in Doppler-radar observations (Browning *et al*., 2001). This profile is chosen as one for which multiple slantwise circulations can occur, but the aim of these idealized experiments is not directly to simulate the circulations observed. The profile used (Figure 1) incorporates the slightly stable boundary layer, capping inversion and moist troposphere observed. (An idealized profile based on this observed case was also used by Pizzamei *et al*. (2005) in their cloud-resolving model simulations (see figure 2 in their paper). The profile used here differs in that the depth of the inversion has been reduced to more closely match that observed (the deep inversion used by Pizzamei *et al*. led to unrealistically deep line convection, reaching 450 mb, in this model), and the relative humidity was reduced slightly to 85% near the surface (the 95% relative humidity used by Pizzamei *et al*. led to noisy relative-humidity fields).)

The along-front jet consists of a westerly wind increasing from zero at the surface to a maximum value $u_{\max} = 25\ \mathrm{ms}^{-1}$ at the tropopause (at around 10 km). The vertical wind shear is specified to be a constant value k in the lowest 2 km, decreasing linearly to zero at a specified height z_{shear} defined by

$$k = \frac{2u_{\max}}{2000\ \mathrm{m} + z_{\mathrm{shear}}}.$$

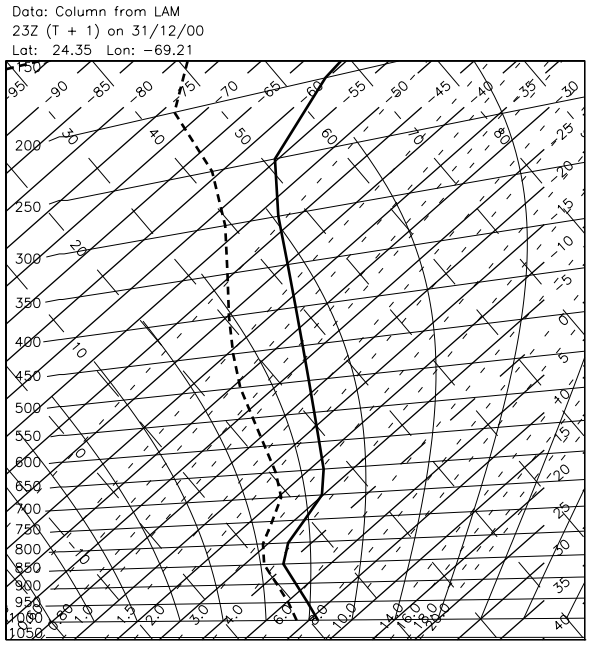

Figure 1. Tephigram of the initial atmospheric profile at the midpoint of the domain (solid line is temperature, dashed line is dew point temperature.

If z_{shear} is less than 10 km, the wind speed is then constant until 10 km. Above z_{shear} (or 10 km, whichever is the greater), the wind speed decreases linearly, reaching zero at 16 km. For the control simulation, $k = 0.005\ \mathrm{s}^{-1}$, yielding $z_{\mathrm{shear}} = 8$ km. The peak jet speed is about half that observed (54 ms^{-1} at 8 km). This reduced speed is necessary to avoid inertial instability in the initial conditions. The relatively strong wind shear at low levels enables the adjustment of circulations in response to the baroclinicity (the ΔM-adjustment process) despite the relatively low peak jet speed, and is consistent with the concept of a low-level jet as observed on 10 February 2000 (Browning *et al*., 2001). In the meridional direction, the jet structure is given by

$$u(y, z) = \frac{u_0(z)}{2}\left(1 - \cos\frac{(y + W/2)\pi}{W/2}\right).$$

Here $u(y, z)$ is the zonal wind; y is the meridional distance relative to the centre of the domain; $u_0(z)$ is the maximum zonal wind at height z; and W is the jet width (700 km). The resulting jet structure is shown in Figure 2(a). The meridional temperature gradient is calculated from the thermal-wind relationship, and is added to the model temperature and sea-surface-temperature fields, yielding higher temperatures to the south of the domain and lower temperatures to the north.

A deformation-strain field is applied to the front, given by the stream function $\psi = -\alpha xy$, where α is a constant strain rate. The deformation field is constant from the surface to 5 km, and decreases smoothly to zero at 10 km, following a tanh function. Above this height, the deformation-wind strength is zero. The deformation-wind field is constant in time. It is added to the jet-wind field in the initial conditions (the initial deformation

DOI: 10.1002/qj

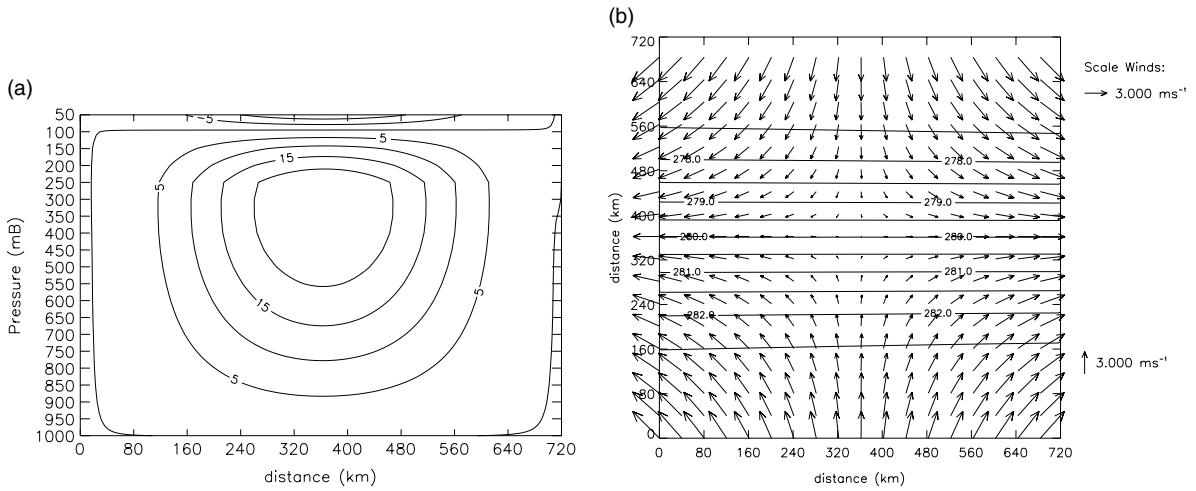

Figure 2. Initial conditions for the control simulation: (a) vertical section showing the zonal wind (ms^{-1}); (b) wet-bulb potential temperature (K) plotted with wind vectors for the deformation field (both at 1000 mb).

field and wet-bulb potential-temperature field at 1000 mb are plotted in Figure 2(b)). The model has fixed lateral boundaries, and is forced from the boundaries by calculating the strength of the deformation strain and the corresponding pressure at each time step as described in Dacre and Gray (2006).

3. Methodology

3.1. Model simulations

A series of model simulations is performed to address the objectives described in Section 1. The model parameters varied are: the strength of the deformation strain; the representation of convection; and the strength of the low-level baroclinicity as specified by the vertical wind shear (Table I).

The deformation-strain rate is varied between 0.6×10^{-5} s^{-1} and 1.4×10^{-5} s^{-1}. Values of environmental deformation-strain rate for observed frontal-wave cases typically lie within this range, or are weaker (as determined using the domain-independent vorticity-and-divergence-attribution method of Bishop and Thorpe (1994a, 1994b) by Renfrew *et al.* (1997), Rivals *et al.* (1998), Chaboureau and Thorpe (1999) and Patoux *et al.* (2005)). Weaker deformation strains failed to trigger frontal convection in the model within a reasonable time period.

Table I. Specification of model simulations.

Label	Deformation rate (10^{-5} s^{-1})	Convective parametrization	Low-level vertical wind shear (s^{-1})
CONTROL	1.0	off	0.005
WEAK_DEF	0.6	off	0.005
STRONG_DEF	1.4	off	0.005
CONV_ON	1.0	on	0.005
CONV_ON_WEAK_DEF	0.8	on	0.005
CONV_MOD	1.0	modified	0.005
WEAK_SHEAR	1.0	off	0.004
STRONG_SHEAR	1.0	off	0.006

The basic premise of convective-parametrization schemes (that a grid box contains many clouds) is not valid at the grid spacing used (4 km), but the model is only able to revolve the coarsest features of (relatively large-scale) clouds. This dilemma is currently being addressed by operational high-resolution numerical weather-prediction models. The effects of three possible representations of convection are examined here: explicit convection (no parametrization scheme); parametrized convection using the mass-flux scheme of Gregory and Rowntree (1990); and a modified version of this convection scheme, developed by Roberts (2003), that avoids the accumulation of high values of convective available potential energy (CAPE) at the grid scale (which can lead to unphysical 'grid-point storms'). The scheme of Gregory and Rowntree (1990) has a trigger dependent on the initial parcel buoyancy, and a mass-flux determined by a specified time-scale for adjustment of CAPE (set here to the typical value of 30 min). In the modified scheme, the CAPE-adjustment time-scale is specified as an increasing function of CAPE; this ensures that the largest values of mass flux occur at the smallest spatial scales (i.e. where the CAPE is largest). This modified scheme is currently used in the operational 4 km version of this model. The default (control) representation of convection presented here is that in which the convective parametrization is turned off. This choice is based on the findings of simulations with these different representations of convection (described in Section 4.4).

Finally, the low-level shear is increased and decreased from its control value. This addresses the sensitivity of the evolution to the (initial) strength of the front, as defined by its low-level baroclinicity. Note that the baroclinicity will change as the deformation field acts on the front.

DOI: 10.1002/qj

3.2. Diagnostics

CSI, ΔM adjustment and density currents need to be identified in the model simulations. The diagnostics used are described here.

CSI is a type of MSI. Regions where MSI can be realized are identified using diagnostics based on the 'vertically-integrated extent of realizable symmetric instability' (VRS) diagnostic of Dixon *et al*. (2002). The VRS diagnostic gives the vertical extent of the regions in the model where the atmosphere has MSI that can be realized. Regions where the moist potential vorticity (MPV) is negative are determined (a criterion for MSI), with added constraints that remove regions that are also convectively or inertially unstable (alternative causes of negative MPV). Sufficient moisture and lift are also required, so that the MSI can be realized. The criteria applied here to determine regions of realizable MSI are:

- negative $MPV < 0$;
- convective stability – positive moist static stability;
- cloud – relative humidity greater than 95%;
- ascent – positive vertical velocity;
- inertial stability – positive absolute vorticity.

Grid points at which the above criteria are met are classed as points with realizable slantwise instability (RSI). We will assume in this paper that moist ascent in a region of slantwise instability (i.e. a region of RSI) is evidence of the release of that slantwise instability. Dixon *et al*. (2002) defined the VRS diagnostic as the number of levels between 1000 mb and 50 mb (with a 50 mb interval) at which the RSI criteria are met. Thus the VRS diagnostic shows the vertically-integrated extent of the regions where MSI can be realized. This represents an advantage over the more commonly used slantwise CAPE (SCAPE) diagnostic, which only shows regions unstable to MSI by parcel ascent from a single origin level. However, the disadvantage of the VRS diagnostic is that, unlike SCAPE, it does not give any measure of the degree of instability. Note that the constraint on relative humidity is subjective (here we use the same value as Dixon *et al*. (2002)). A less strict constraint (e.g. relative humidity exceeding 90%) yields larger regions satisfying the RSI diagnostic, so that our estimates of MSI release could be considered conservative. However, this does not affect the overall conclusions drawn in this paper.

Convective stability is measured using the moist static stability calculated using the formula given in Durran and Klemp (1982). This is the static stability for a saturated atmosphere, so the MSI defined by these criteria is CSI (rather than potential symmetric instability – see Schultz and Schumacher (1999) for an explanation of the differences between these two types of MSI). Absolute vorticity is calculated on isobaric surfaces. Strictly speaking, the absolute vorticity and RSI (through the MPV term) should both be calculated using geostrophic rather than full winds (as explained by Schultz and Schumacher (1999) and implemented by Dixon *et al*. (2002)). However, the geostrophic wind (derived from the geopotential height) was found to be unacceptably noisy because of grid-scale pressure fluctuations arising from gravity waves, so the full wind is used instead. Shutts (1990) also found model geostrophic winds to be unacceptably noisy. He therefore used the full winds, rather than just the geostrophic component, to calculate CSI (via the SCAPE diagnostic). Further references relating to the sensitivity of the calculation of MPV to the use of the full versus the geostrophic winds can be found in Novak *et al*. (2006, section 3b(3)).

Regions where slantwise adjustment is occurring because of the ΔM-adjustment process are identified as regions where there is inertial instability. These can be diagnosed as regions of negative absolute vertical vorticity for positive (Northern-Hemisphere) Coriolis parameter (e.g. Knox, 2003). By using inertial instability as our diagnostic for ΔM adjustment, we assume here that this inertially-unstable region is generated by vertical ascent (either forced or through the release of convective instability) in a baroclinic environment (the definition of Fischer and Lalaurette (1995b)). Xu (1986a, 2004) has shown that the release of two-dimensional CSI ($\partial/\partial y = 0$) can generate localized regions of negative $\partial v/\partial x$ (and hence potentially negative $\zeta = f + \partial v/\partial x$) on the cold side of the upper part of the generated circulation. This suggests that the release of CSI may theoretically generate localized regions of inertial instability, and this possibility must be excluded from our analysis.

Density (or gravity) currents arising as spreading low-level cold pools generated by convection are identified as localized regions of reduced virtual potential temperature θ_v. This is (very nearly) a conserved variable in unsaturated air, and directly related to density. A comparison of two air masses (at the same pressure) with differing θ_v thus gives a comparison of their densities. The speed of a density current is proportional to the square root of the difference in θ_v between the density current and the environment (e.g. Droegemeier and Wilhelmson, 1985). Smith and Reeder (1988) note that 'when precipitation occurs at, or near, the front, the "front" is likely to be reinforced at the surface by cold air outflow associated with the evaporation of precipitation and could be expected to have the local structure of a gravity current'.

4. Results

4.1. Evolution of control simulation

The evolution of frontal convection and the mechanisms driving it are described here for the control simulation (CONTROL – see Table I). The triggering of line convection and development of a wide frontal rain band to the cold-air side (north) of the line convection are depicted by means of the evolution of relative humidity at 750 mb (Figure 3). Convection (defined here as relative humidity exceeding 90%) is triggered along the surface front at about 10 h into the simulation. This triggering occurs

DOI: 10.1002/qj

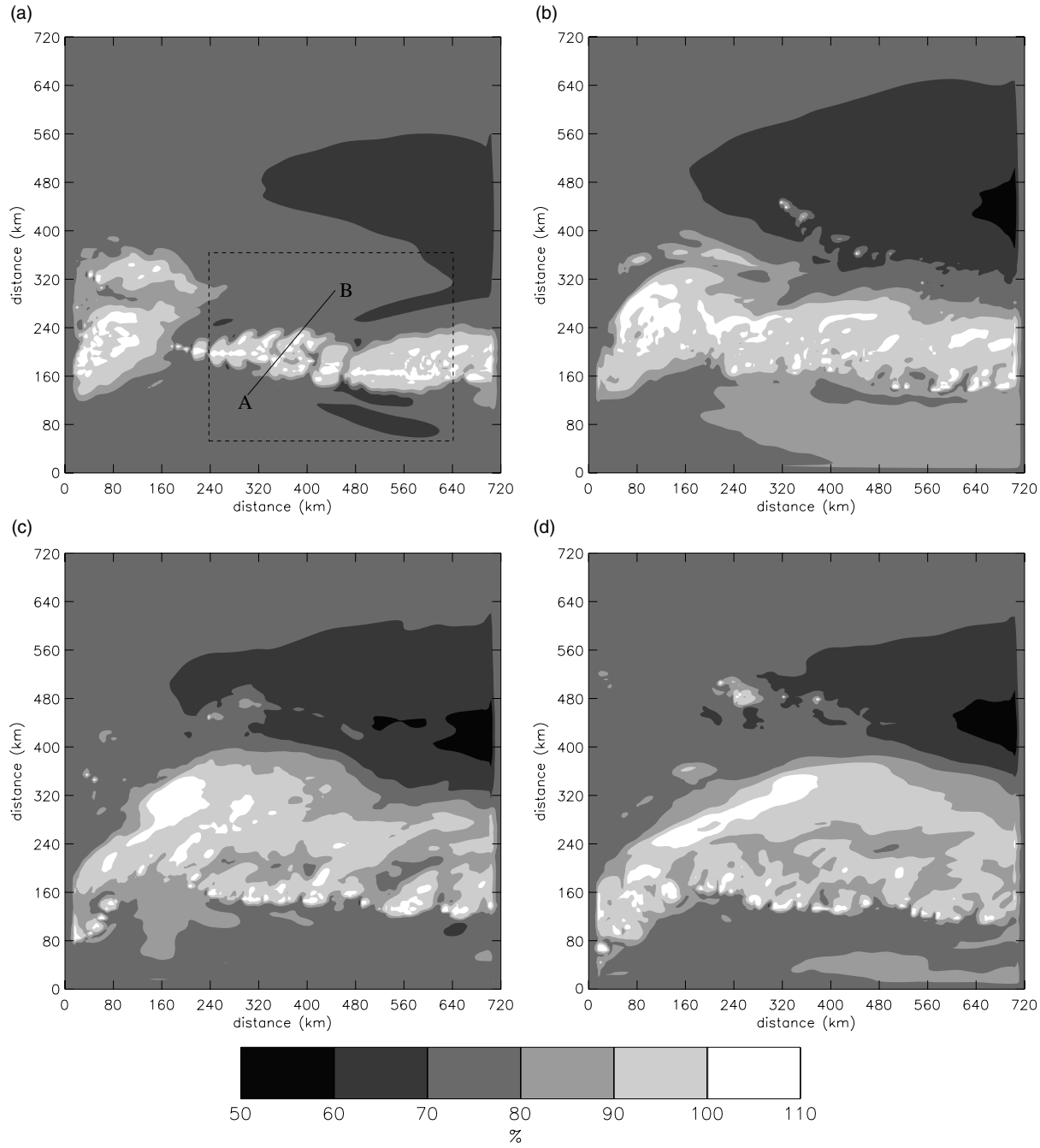

Figure 3. Relative humidity at 750 mb, for the control simulation (CONTROL), after: (a) 15 h; (b) 20 h; (c) 25 h; (d) 30 h. The dashed box in (a) shows the domain used for the Hovmüller plots (Figures 5 and 8) and for Figures 6 and 10. The solid line A–B in (a) shows the location of the cross section plotted in Figure 4.

initially on the east side of the domain, but by 15 h convection has been triggered across the entire domain (Figure 3(a)). The surface winds are strongest to the east of the domain, because of the combined effects of the deformation field and the zonal jet. The profile moistens at low levels as surface fluxes enhance instability. The more rapid moistening to the east of the domain causes the convection to be initiated there within the band of highest low-level specific humidity that lies parallel to the front (CAPE values are about 160 J kg^{-1} in the region of triggering, slightly less than the peak values of about 210 J kg^{-1} lying in a band to the south of this). The broad convection region along the western boundary of the domain (within 160 km of that boundary at 15 h) is not frontal in nature. It is triggered along that boundary by circulations that develop from inconsistencies due to the fixed lateral boundary conditions (these inconsistencies were also noted by Dacre and Gray (2006) using a very similar model configuration). It slowly moves into the domain, and will be neglected when addressing the questions posed in this study. The narrow rain band of intense convection (highest relative humidity) comprising the line convection is coherent across the domain, but can be seen to be composed of shorter line elements. This

DOI: 10.1002/qj

breakup into line elements is characteristic of line convection, and is in nature attributed to horizontal shearing instability on the strongly-sheared edge of the low-level jet that occurs ahead of the front (James and Browning, 1979; Hobbs and Biswas, 1979). Explicit representation of convection in mesoscale models also leads to a tendency for convection to appear more discretized.

Regions of cloud can be seen to extend northeastwards from the frontal line elements, resulting in frontal bands (Figure 3(a)). This is anticlockwise from the direction of the westerly thermal wind. As the simulation evolves, these form a broad region of cloud to the north of the line convection (Figure 3(b)). At later times, this cloud band appears to be separated from the line convection at this level by a region of reduced relative humidity (Figure 3(c,d)). The line convection remains active throughout the time period shown in Figure 3, as it can be continuously identified as a region of very high relative humidity. The line moves slowly southwards during the period shown (by about 30 km over 15 h).

The mechanism leading to the formation of frontal bands is identified by examining the evolution of one of these bands (Figure 4). The location of the cross section plotted is marked on Figure 3(a). The cross sections show regions of cloud, ΔM adjustment and CSI release at hourly intervals, using the diagnostics of relative humidity, absolute vorticity and RSI respectively (the latter two diagnostics are defined in Section 3.2). Grid points satisfying the criteria for RSI are labelled with the value 1 (grid points not satisfying the criteria have the value zero), but the contour shown corresponds to 0.1, to allow for the interpolation necessary to produce these oblique cross sections and to emphasize the small-scale regions satisfying this diagnostic. This explains why there are regions of RSI that overlap with inertially-unstable regions in these cross sections, despite the requirement that grid points satisfying the RSI diagnostic be inertially stable.

Note that during this period the band does not have a significant component of motion normal to the cross section shown. At 14 h, there are two upright clouds, separated by a region of relatively dry air due to evaporatively-driven convective downdraughts (Figure 4(a)). Note that the top of the convection reaches 600 mb, the level of the inversion in the local thermodynamic profile (this is slightly higher than the inversion in the initial conditions at the centre of the domain, Figure 1); this inversion thus caps the cloud.

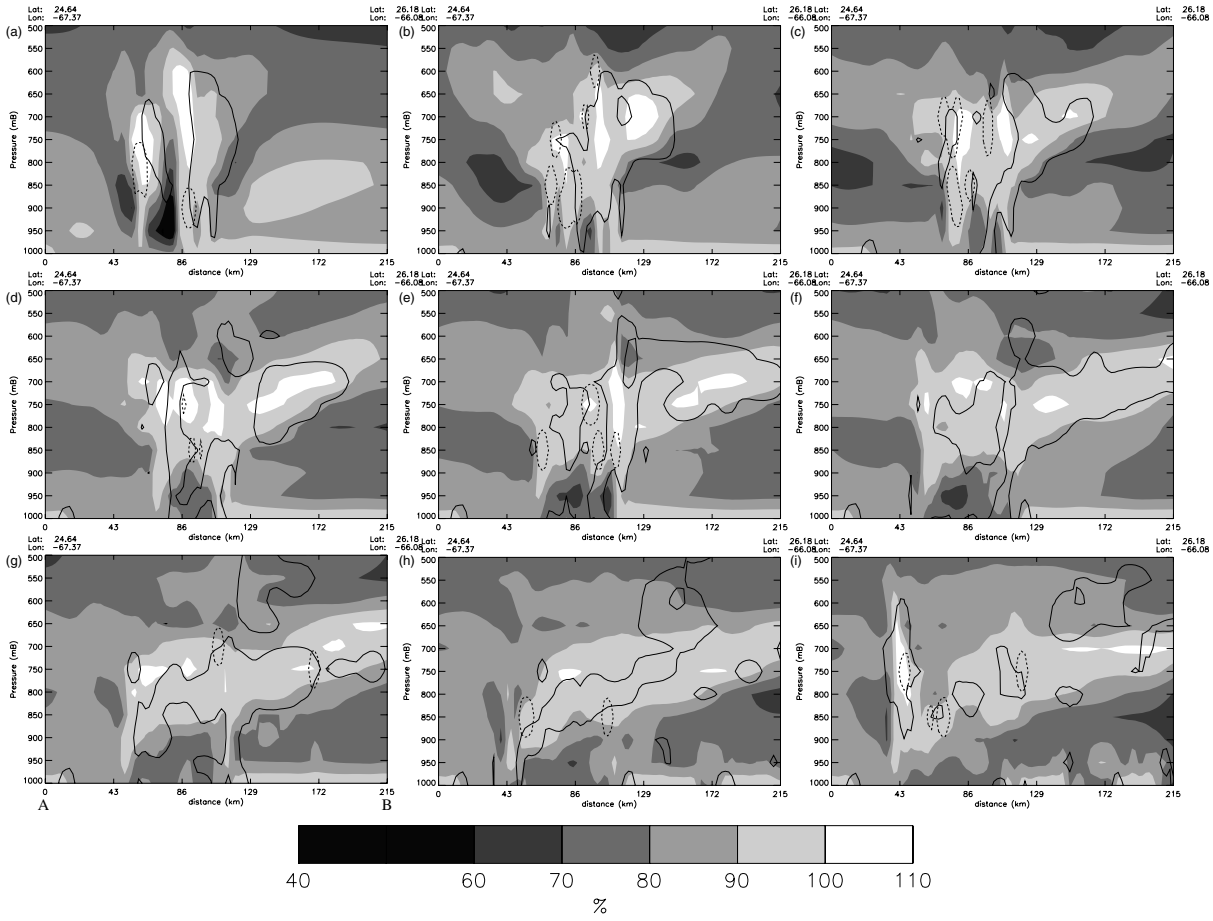

Figure 4. Vertical cross sections of relative humidity (shading), ΔM adjustment (solid contour indicates zero absolute vorticity) and CSI release (dashed contour shows regions satisfying the criteria of the RSI diagnostic – the contoured value is 0.1 because of the interpolation necessary for the cross section), for the control simulation (CONTROL) at hourly intervals from (a) 14 h to (i) 22 h. The location of the cross section is marked in Figure 3(a); the limits of the cross section (A and B) are marked on panel (g).

DOI: 10.1002/qj

These clouds merge to form a continuous cloud band at mid-levels, and a slantwise extension occurs towards the cold air (right-hand side of sections, Figure 4(b)). The base of the right-hand cloud moves into the cold air (Figure 4(a–h)), with a reinvigoration at 18 h (Figure 4(e)) associated with an enhancement of the low-level relatively-dry air, before becoming detached from the surface at 22 h (at least in this cross section, Figure 4(i)). The base of the left-hand cloud moves towards the warm air (left-hand side of sections) during the period shown, though not continuously, and is reinvigorated at the end of this period (Figure 4(i)). The slantwise extension of the cloud band is occurring in an inertially-unstable region arising from subgeostrophic momentum anomalies. The large coherent regions of inertial instability, co-located with the entire slantwise-ascending region, appear to have been generated by upright ascent in the baroclinic zone, so satisfying the definition of the ΔM-adjustment process. These inertially-unstable regions are stable to moist instability (not shown). Grid points satisfying the RSI diagnostic exist, but, unlike the grid points with inertial instability, they do not form coherent regions co-located with the slantwise cloud. This implies that ΔM adjustment is the mechanism leading to the slantwise extension of the cloud band (as found in the model simulations of Fischer and Lalaurette (1995b) and Pizzamei *et al*. (2005)).

The relationship between the low-level vertical motion and cold pools formed by evaporating downdraughts driven by the convection is explored using Hovmüller plots of vertical velocity w and of θ_v (Figure 5). These plots show how the zonally-averaged fields evolve with time in the cross-frontal direction. The advantage of performing zonal averaging is that variability due to individual convective plumes and line elements is smoothed; the disadvantage is that apparent multiple banding in the w plots must be treated with caution, as the frontal convection is not entirely zonal but composed of line elements that are meridionally separated (Figure 3). The zonal averaging is performed across the region marked by the dashed box in Figure 3(a). The deformation field leads to a slow strengthening of the front, and strong ascent is triggered at 11 h. This ascent is co-located with convection (not shown). Triggering occurs on the warm edge of the strong θ_v gradient, and thus along the line where the front would be analysed. By 14 h, a cold pool has been generated at the surface (as seen by the rapid cooling in the region of strong ascent). This cold pool spreads in the cross-frontal direction with time. This spreading is more clearly seen towards the warm air, because of the enhancement of the temperature gradient, but it also occurs towards the cold air, as can be seen by a reduction in the speed of southerly advancement of the cold air. The cold pool dissipates at about 24 h. The line convection that generates the cold pool appears as two strong ascent regions 20–30 km apart that move towards the warm air between about 15 h and 30 h. This apparent double band is a consequence of the zonal averaging. A signal can also be seen moving towards the cold air. This signal is initially one of strong ascent, but over time it becomes a noisy signal of ascending and descending regions. This ascent is ahead of and driven by the spreading cold pool, as seen in the cross sections shown in Figure 4. This movement stops at about 24 h, at a cross-frontal distance of about 260 km, after which time a broad band of weak ascent moves from this point towards the warm air. This ascent is associated with an outbreak of shallow upright convection (about 1 km deep) until near the end of the simulation, when it becomes adjacent to the line convection and associated with a low-level slantwise band (see Section 4.2 for more details). Finally, the rapidly-moving signals primarily of descent (but also of slightly less coherent ascent) moving into both the cold and the warm air can be attributed to gravity waves. These are moving at speeds of about 13 ms^{-1} in this simulation.

4.2. Sensitivity to deformation strain

Key features of the sensitivity of the frontal precipitation to deformation-strain rate are shown by the evolution of the average rainfall rate over the frontal region (Figure 6). An initial burst of intense rainfall occurs in the three simulations shown in which the convective-parametrization scheme is not active (CONTROL, STRONG_DEF and WEAK_DEF).

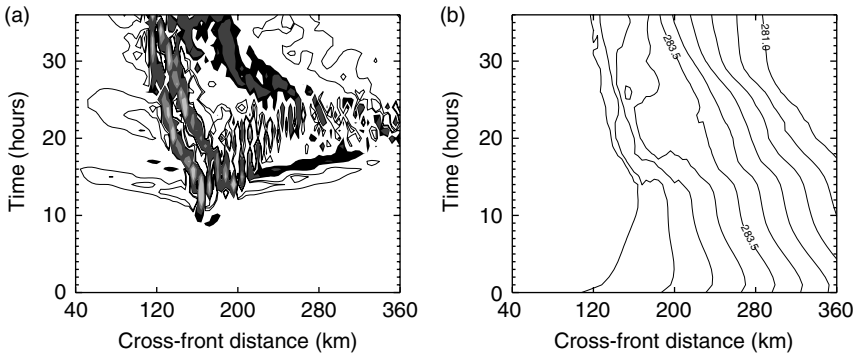

Figure 5. Hovmüller plots, for the control simulation (CONTROL), of: (a) vertical velocity at 250 m (ascent shown by filled contours at 0.005 ms^{-1}, 0.01 ms^{-1}, 0.05 ms^{-1}, 0.1 ms^{-1} and 0.5 ms^{-1}, and descent shown by unfilled contours at -0.1 ms^{-1}, -0.05 ms^{-1}, -0.01 ms^{-1} and -0.005 ms^{-1}); (b) virtual potential temperature at the lowest model level (31 m) (contour interval 0.5 K). The plot is calculated by assuming a zonal front and averaging across the region 240–640 km in the along-front direction (the domain is marked in Figure 3(a)).

DOI: 10.1002/qj

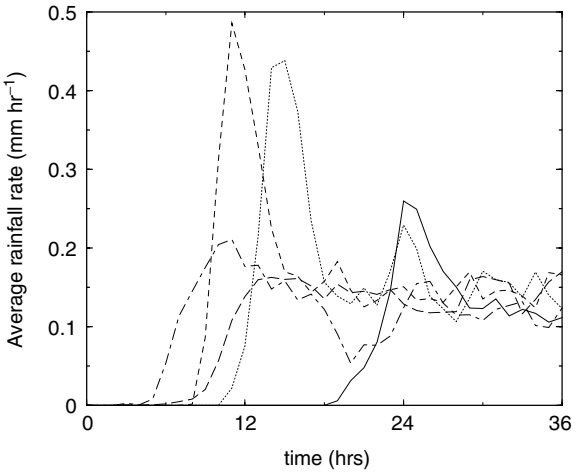

Figure 6. Time series of the area-averaged precipitation rate (parametrized plus explicitly-resolved) within the region 240–640 km (zonal direction) by 40–360 km (meridional direction) (total of 8181 grid points – domain marked in Figure 3(a)). Simulations are those with deformation rates of 1.4×10^{-5} s^{-1} (STRONG_DEF, short-dashed line), 1.0×10^{-5} s^{-1} (CONTROL, dotted line), 0.6×10^{-5} s^{-1} (WEAK_DEF, solid line), 1.0×10^{-5} s^{-1} with convective-parametrization scheme active (CONV_ON, long-dashed line), and 1.0×10^{-5} s^{-1} with modified convective-parametrization scheme active (CONV_MOD, dash-dotted line).

After about 6 h, this burst dies away and a relatively constant average rainfall rate occurs. This relatively constant rate is similar for all the simulations shown (independent of the deformation rate applied and convective parametrization). The dependence of the banded frontal clouds on the representation of convection in the model is discussed in Section 4.4. The timing of the onset of precipitation is strongly controlled by the deformation rate applied, with a stronger rate leading to earlier onset. This is a consequence of the stronger low-level winds, which lead to a more rapid moistening of the low-level thermodynamic profile.

The cloud bands formed are more coherent in the presence of stronger deformation-strain rate. Figure 7 shows the relative humidity at 750 mb for the simulations with deformation-strain rates of 1.4×10^{-5} s^{-1} (STRONG_DEF) and 0.6×10^{-5} s^{-1} (WEAK_DEF), for comparison with the control simulation (CONTROL) shown in Figure 3. The times selected for Figure 7 are just after the peak in the initial burst of rainfall (see Figure 6) for the corresponding simulations, and thus should be compared to the control simulation at the time shown in Figure 3(a). The later onset of convection for weaker strain rates results in a larger proportion of the domain being affected by the broad convective feature that advects in from the western boundary. However, line convection and a wide frontal cloud band (predominantly to the cold-air side of the line convection) can be seen in all three simulations. The banding is more zonal in nature in the simulations with higher strain rates, and appears somewhat less broken up into individual line elements.

The effect of changing the strain rate on the movement of the bands and the associated cold pools can be seen by comparing the Hovmüller plots of w and θ_v calculated for the CONTROL and STRONG_DEF simulations, shown in Figures 5 and 8 respectively. The corresponding Hovmüller plot for the WEAK_DEF simulation is not calculated, as the cloud band is not zonally coherent over the averaging region chosen and the late onset of convection limits the time over which the bands can be studied. The same basic features are present in both Hovmüller plots: convective triggering (inferred from strong ascent) shortly followed by the generation of a surface cold pool

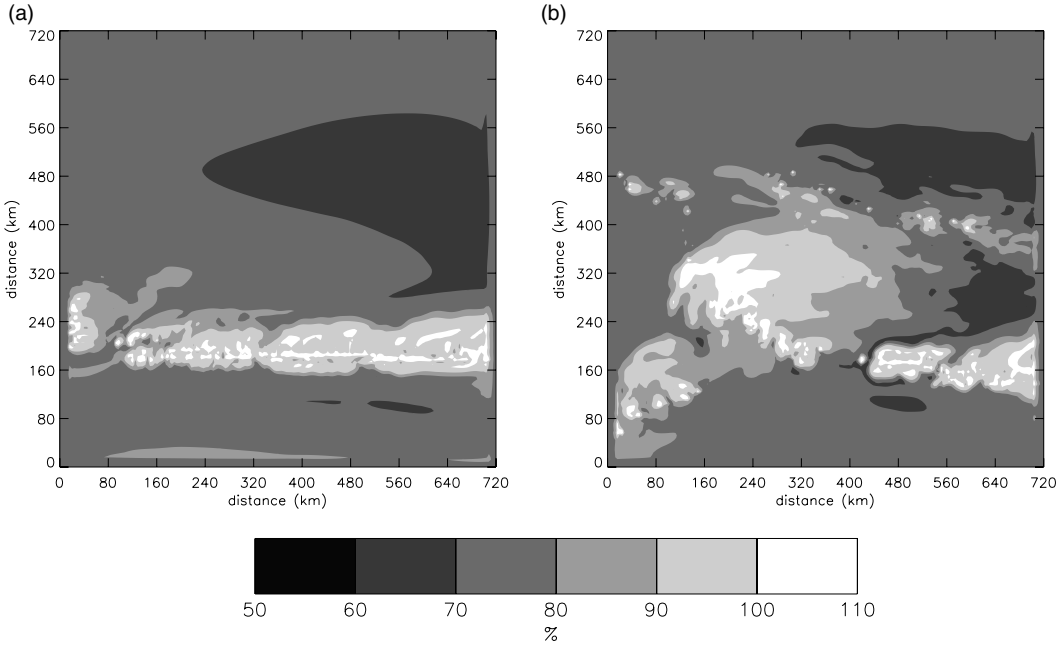

Figure 7. Relative humidity at 750 mb, for the simulations with: (a) a deformation rate of 1.4×10^{-5} s^{-1} (STRONG_DEF) after 12 h; (b) a deformation rate of 0.6×10^{-5} s^{-1} (WEAK_DEF) after 25 h.

DOI: 10.1002/qj

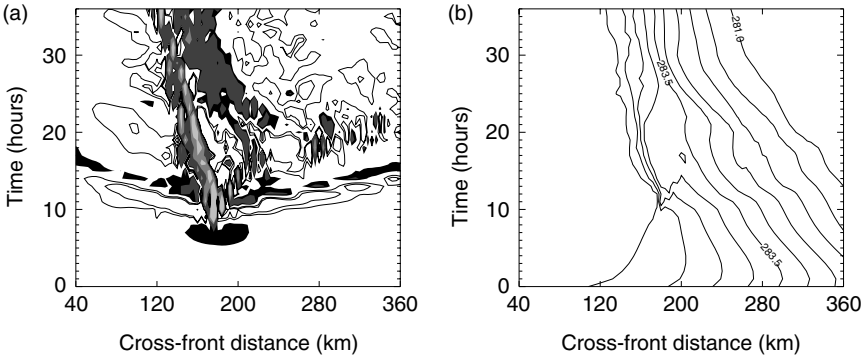

Figure 8. As Figure 5, but for the simulation with a deformation rate of 1.4×10^{-5} s^{-1} (STRONG_DEF).

that spreads in the cross-frontal direction; movement of the main convective band into the warm air; some short-term convective-band movement into the cold air; and rapidly-moving gravity waves. The stronger strain rate leads to the more rapid contraction of the θ_v contours (frontogenesis) seen in Figure 8(b). Consequently, triggering occurs slightly further north in the simulation with stronger strain rate. The cold pool triggered in this simulation is more intense (the θ_v gradient is stronger) and longer-lasting. However, the speed of the main convective band (and cold pool) is less in the simulation with stronger deformation. Estimates of the cloud-band speeds during the time when the strong cold pool is present are 0.6 ms^{-1} and 1.0 ms^{-1} for the STRONG_DEF and CONTROL simulations respectively (from Figures 5(a) and 8(a)). This result appears to contradict the theoretical proportionality between the speed of a density current and the square root of the difference in θ_v between the density current and the environment (for otherwise-similar cold pools) stated in Section 3.2. This suggests that there are two competing processes controlling the cold-pool spreading: on the one hand, a stronger deformation rate generates more intense convection, leading to a more intense cold pool that spreads faster; and on the other hand, a stronger deformation rate inhibits the cold pool from spreading through stronger low-level cross-frontal convergence. In these simulations, the latter processes wins. This hypothesis is confirmed by experiments with different low-level shear, described in Section 4.3.

Multiple bands of precipitation form in the simulation with the strongest strain rate (STRONG_DEF, Figure 9). At 19 h, two bands of precipitation exceeding 100 km in length exist parallel to and to the north of the line convection. The band spacing is about 60 km, which is within the large range measured in observational studies (e.g. Lagouvardos *et al*., 1993, table 1). The signature of these bands can also be seen in the Hovmüller plot of w (Figure 8). The more northerly band persists for only about 2–3 h (in w and in precipitation (not shown)). The mechanism that triggers this band is not clear. The middle band forms along, and moves with, the northern edge of the expanding cold pool that is generated by the line convection. It is distinguishable from the line convection (as a distinct precipitation band) at about 15 h, and moves northwards until about 18 h, before dissipating at about 21 h (at a cross-frontal distance of about 220 km and about 50 km north of the line convection). A band of precipitation moving with the cold pool is also seen with weaker strain rates (for example, in the CONTROL simulation), but a third band is not seen in these simulations.

The role of the release of CSI in the simulations is quantified by determining the evolution of the total number of grid points (in the banding region) satisfying the RSI diagnostic (Figure 10). This is determined for simulations with five values of the strain rate, ranging from 0.6×10^{-5} s^{-1} to 1.4×10^{-5} s^{-1}. Vertically, the RSI diagnostic is calculated on 20 pressure levels spaced 50 mb apart. The onset of convection (as shown by the time series of precipitation in Figure 6) occurs at the same time as the generation of realizable CSI (as measured by the number of points satisfying the RSI diagnostic). This is then maintained at an approximately constant value – a

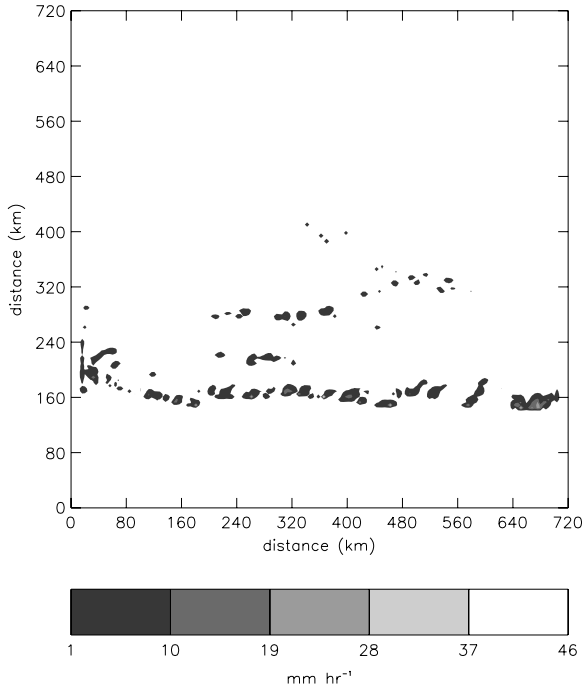

Figure 9. Rainfall rate for the simulations with a deformation rate of 1.4×10^{-5} s^{-1} (STRONG_DEF) after 19 h.

DOI: 10.1002/qj

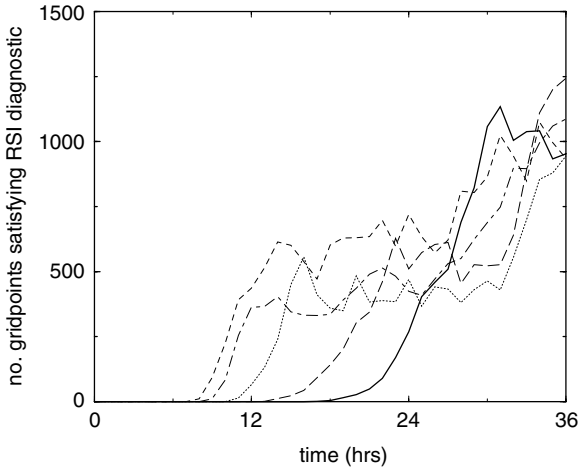

Figure 10. Time series of the number of grid points satisfying the RSI diagnostic within the depth of the atmosphere (calculated on pressure levels spaced every 50 mb between 1000 mb and 50 mb) and the region 240–640 km (zonal direction) by 40–360 km (meridional direction) (total of 8181 grid points – domain marked in Figure 3(a)). The simulations are those with deformation rates of 1.4×10^{-5} s^{-1} (STRONG_DEF, short-dashed line), 1.2×10^{-5} s^{-1} (dash-dotted line), 1.0×10^{-5} s^{-1} (CONTROL, dotted line), 0.8×10^{-5} s^{-1} (long-dashed line), and 0.6×10^{-5} s^{-1} (WEAK_DEF, solid line).

plateau stage – before increasing towards the end of the simulations (the onset of the increase ranges between about 27 h and 32 h). Note that the inertial instability is remarkably consistent between the different simulations beyond 24 h for simulations with varying low-level shear (see Figure 12(b)) and deformation rate (not shown). The period of constant RSI coincides with the time when the line convection is active (as inferred from the presence of the cold pool, seen in Figures 5 and 8, for example). For the WEAK_DEF simulation, the number of points satisfying the RSI diagnostic does not go through a plateau stage, but gradually increases to a value similar to those of the other simulations. The summed RSI is very similar at the end of all five simulations.

The summed RSI diagnostic shows a consistent evolution for all the simulations, independent of the strain rate. However, this simple summation does not provide information on the spatial distribution of grid points satisfying the RSI diagnostic. It is more likely that the release of CSI will result in slantwise circulations if there are coherent regions (rather than isolated grid points) satisfying this diagnostic. There are no coherent regions satisfying the RSI diagnostic in the vertical cross sections taken from the CONTROL simulation shown in Figure 3. However, coherent low-level regions satisfying the RSI diagnostic develop towards the end of all the simulations represented in Figure 10, coinciding with an increase in the number of grid points satisfying this diagnostic. These coherent regions can be seen in the top panels of Figure 11 for the stronger-deformation simulation (STRONG_DEF). They form

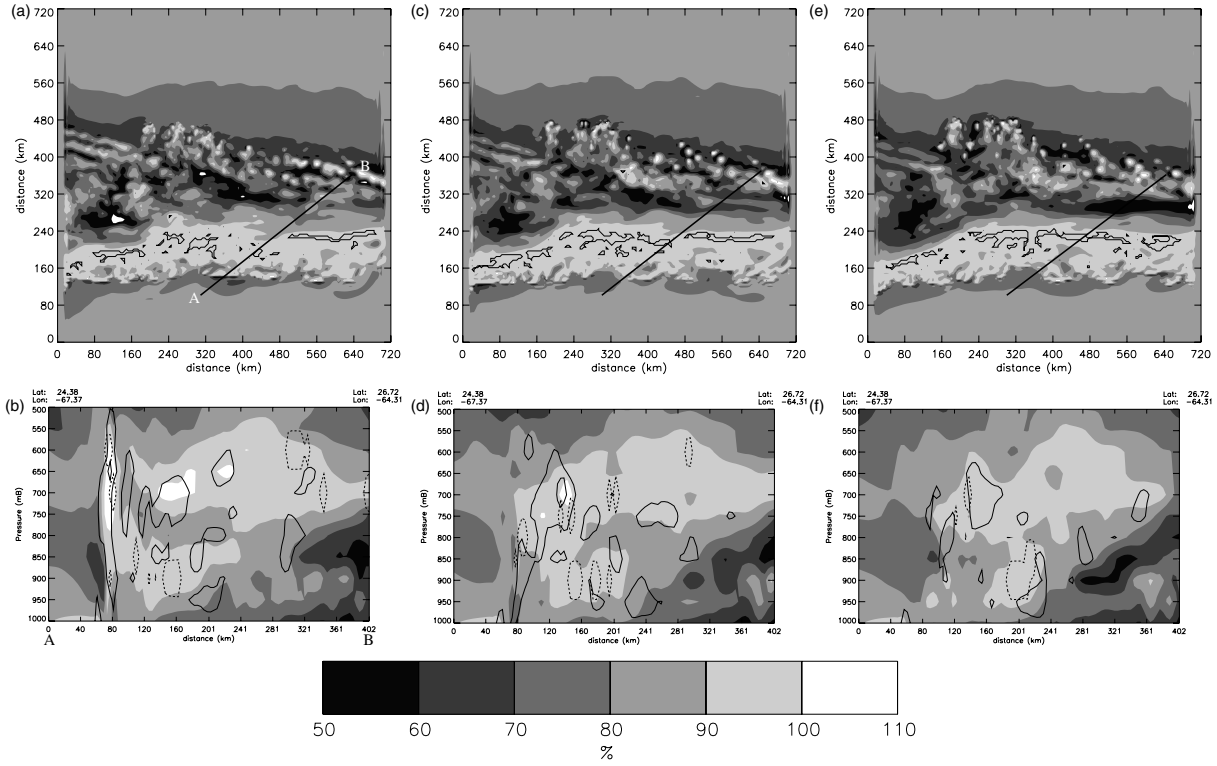

Figure 11. Horizontal sections at 900 mb at (a) 28 h, (c) 30 h and (e) 32 h, and vertical cross sections at (b) 28 h, (d) 30 h and (f) 32 h, for the simulation with a deformation rate of 1.4×10^{-5} s^{-1} (STRONG_DEF), showing relative humidity (shading), ΔM adjustment (solid contour corresponding to zero absolute vorticity in the lower panels only), and CSI release (contours showing regions satisfying the criteria of the RSI diagnostic, with contoured values of 1 for horizontal sections (solid contours) and 0.1 for vertical sections (dashed contours) because of the interpolation necessary for the cross sections). The location of the cross section is marked on the upper panels, and labelled A–B in panel (a). The limits (A and B) are marked beneath panel (b).

DOI: 10.1002/qj

a line to the cold-air side of the line convection at around 900 mb, and are associated with a cloud band that forms below the main slantwise-ascending band extending from the line convection (bottom panels of Figure 11). The main slantwise-ascending band occurs in an inertially-unstable region, and can be attributed to ΔM adjustment (as was also inferred for the control simulation). By contrast, the low-level band occurs in a region that is primarily diagnosed as undergoing CSI release. The evolution of one of the bands is shown between 28 h and 32 h in Figure 11. During this time interval, the cross section shown lies along the same band (the bands are related to discrete line-convection elements along the front). The ascent associated with the low-level bands can be seen immediately to the cold-air side of the strong ascent associated with the line convection in the Hovmüller plots (Figures 5 and 8). The time when weak ascent appears immediately adjacent to the strong ascent is around the time at which the summed RSI diagnostic increases significantly (and at which the low-level bands first appear in the relative-humidity field (not shown)).

4.3. Sensitivity to low-level baroclinicity

The dependence of the movement of the bands and the associated cold pools on the initial strength of the low-level shear can be determined by comparing Hovmüller plots calculated for the WEAK_SHEAR and STRONG_SHEAR simulations (not shown) with that for the CONTROL simulation (Figure 5). The strength of the deformation field is the same in these simulations. Stronger low-level shear is associated with stronger initial cross-frontal gradients in θ_v, as expected from thermal wind balance. It also leads to earlier triggering of convection, enhanced cold pools (stronger θ_v gradients) and more rapid movement of the main convection band (and cold pool) into the warm air (estimated cloud-band speeds during the time when the strong cold pool is present are 0.8 ms^{-1}, 1.0 ms^{-1} and 1.2 ms^{-1} for the WEAK_SHEAR, CONTROL and STRONG_SHEAR simulations respectively). The earlier onset of convection with stronger low-level shear is a consequence of the stronger low-level winds. The hypothesis (proposed in Section 4.2) that stronger strain rates inhibit the spreading of the cold pool (and that this process overcomes the theoretical faster spreading of a more intense cold pool in the absence of deformation strain) is supported by the finding that more intense cold pools do indeed spread faster given the same strain rate.

The strength of subgeostrophic momentum anomalies generated by the line convection is controlled by the low-level shear, since the height of the convection is capped by the mid-level tropospheric inversion (Figure 1). Stronger momentum anomalies are associated with more inertial instability, and thus result in stronger slantwise circulations as that instability is released (ΔM adjustment). This dependence can be seen in time series of the horizontal divergence at cloud top (Figure 12(a)) and the mid-tropospheric inertial instability (Figure 12(b)) for simulations with varying initial low-level shear (but the same deformation-strain rate). Stronger cloud-top divergence (implying stronger slantwise adjustment at cloud top) and stronger inertial instability are both associated with stronger initial low-level shear. Simulations with stronger initial low-level shear also have stronger low-level shear at the time of convective initiation (not shown). Note that the inertial instability peaks at about the time of strongest precipitation (compare the CONTROL time series of precipitation in Figure 6 and inertial instability in Figure 12(b)) before asymptotically approaching an approximately constant value. This reduction in inertial instability implies that it is being released, and hence contributes to the cloud-top divergence. Increased release of CSI may also contribute to the stronger cloud-top divergence found with stronger low-level shear. Figure 12(c) shows a relatively weak but consistent increase in CSI release (as quantified by the number of grid points satisfying the RSI diagnostic) with low-level shear. However, since there are no coherent regions satisfying this RSI diagnostic co-located with the slantwise cloud (as shown for the control simulation in Figure 4), it is likely that ΔM adjustment dominates during the early part of the simulations. This is consistent with the paradigm of slantwise circulations being driven by ΔM adjustment early in the simulations, followed later on by the release of CSI.

4.4. Sensitivity to convective parametrization

The activation of a convective parametrization (in either the standard or the modified form) leads to earlier precipitation onset (for the same deformation-strain rate), with the earliest onset occurring with the modified scheme (Figure 6). This is advantageous as it reduces the extent of the domain contaminated by the artificial features attributed to the fixed lateral boundaries. Unlike in the simulations without a convective-parametrization scheme, an initial rainfall burst does not occur with the standard scheme. A burst is seen with the modified scheme, but of much reduced magnitude compared to the simulations without a convective parametrization. The initial burst of intense rainfall occurs because, in the absence of a parametrization scheme, triggering will not occur until the convective instability has become sufficiently large that showers as large as, or larger than, the grid spacing form. This leads to the buildup of large values of CAPE prior to convection, and delays the onset of convection. The use of a convection scheme prevents this buildup, as it attempts to represent showers on all scales. At onset, the rainfall is mainly attributable to the parametrization scheme. This preconditions the atmosphere in such a way that a rainfall burst does not occur when the convection begins to be resolved explicitly. The modified scheme forces explicit convection in the most unstable regions, and so leads to the explicit representation of some convection that is parametrized with the standard scheme; hence, a small initial burst of rainfall occurs.

DOI: 10.1002/qj

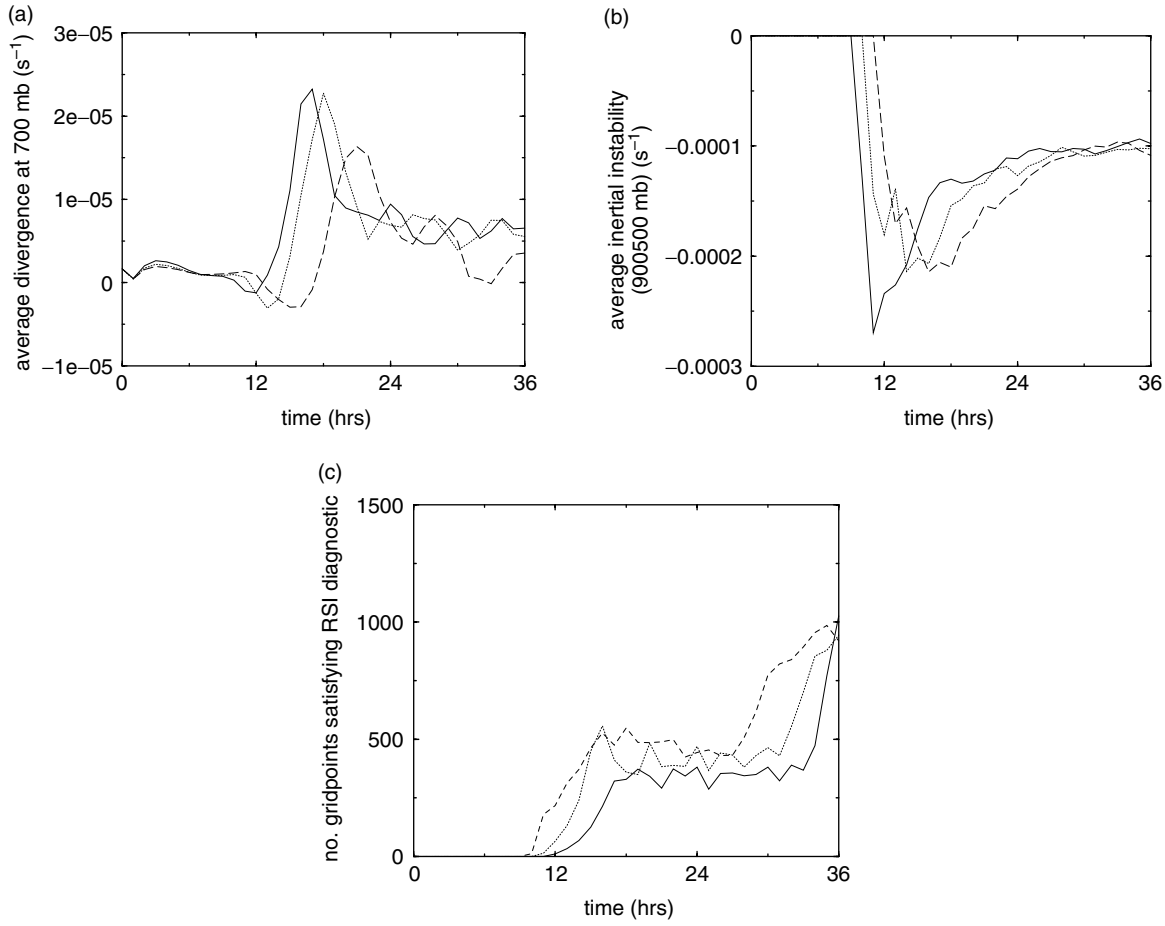

Figure 12. Time series of: (a) average divergence at 700 mb; (b) average inertial instability over levels 900–500 mb inclusive (50 mb interval), calculated as average absolute vorticity for grid points where the absolute vorticity is negative; (c) number of grid points satisfying the RSI diagnostic within the depth of the atmosphere (calculated on pressure levels spaced every 50 mb between 1000 mb and 50 mb). The simulations plotted have different values of initial low-level shear: STRONG_SHEAR (solid line); CONTROL (dotted line); WEAK_SHEAR (dashed line). All panels are calculated for the region 240–640 km (zonal direction) by 40–360 km (meridional direction) (total of 8181 grid points – domain marked in Figure 3(a)).

The analysis of the sensitivity of banded frontal clouds to deformation strain presented in this paper is based on simulations without a convective-parametrization scheme, despite the advantages of using such a scheme, described above. The reason for this is that a known problem with the use of this scheme in this model at this resolution was found to arise (Roberts, 2003; Done *et al.*, 2006). Arcs of precipitation from the convection scheme formed and moved into the warm air. These can be seen by comparing the parametrized (convective) rainfall rate from the CONV_ON_WEAK_DEF simulation at two different times (Figure 13(c)). These arcs are not obvious in the total rainfall rate, as this is dominated by the explicitly-resolved (large-scale) rainfall (Figure 13(b)). However, regions of explicitly-resolved rainfall are co-located with the regions of most intense parametrized rainfall. Hence, the use of a convection scheme also leads to less coherent line convection (compare panels (a) and (b) of Figure 13, which show total rainfall rates at comparable times relative to the peak rainfall rate). Roberts (2003) attributes these arcs to a self-sustaining interaction between the convection scheme and the model dynamics, and finds that they lead to rainfall in the wrong place and incorrectly remove convective instability in case-study simulations. In a case-study simulation using the Unified Model, triggering of the convective scheme was found to cool the atmospheric profile and generate a surface cold pool. Convergence and ascent ahead of this cold pool destabilized the atmosphere and triggered further convection. This cooled the region ahead of the cold pool and advanced it forward. This is a physically reasonable response, but the downdraught cooling occurred too quickly compared to convective clouds in nature, leading to the formation of arcs that were not observed. Bukovsky *et al.* (2006) attributed similar spurious precipitation features to similar mechanisms in the NCEP North American Mesoscale model. These effects are also apparent when using the modified convection scheme (not shown). Hence, despite the delayed and too-intense onset of convection in the simulations without a convection scheme, it was concluded that these simulations were more physically realistic than the equivalent simulations using a convection scheme.

DOI: 10.1002/qj

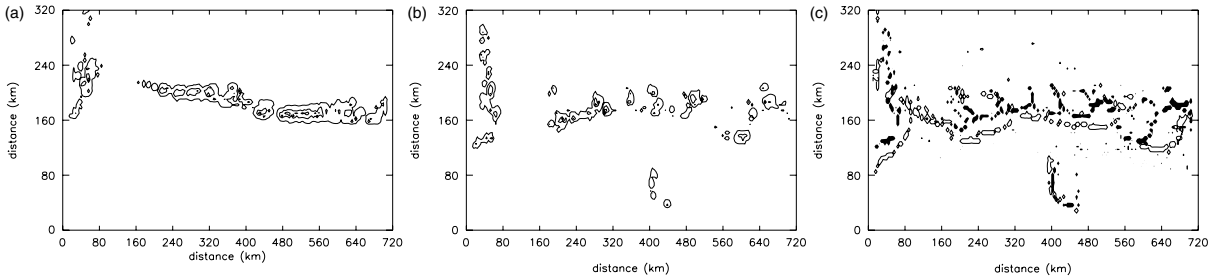

Figure 13. (a) Rainfall rate for the CONTROL simulation at 15 h (contours at 1 mm h^{-1}, 10 mm h^{-1} and 20 mm h^{-1}). (b) Rainfall rate (parametrized plus explicitly-resolved) for the simulation with a deformation rate of 0.8×10^{-5} s^{-1} and with the convective-parametrization scheme active (CONV_ON_WEAK_DEF) at 16 h (contours at 1 mm h^{-1}, 10 mm h^{-1} and 20 mm h^{-1}). (c) Parametrized rainfall rate for the same simulation as shown in (b) at 16 h (shaded for values exceeding 0.2 mm h^{-1}) and 20 h (contour at 0.2 mm h^{-1}). For clarity, only the southern part of the domain is shown (rainfall rates are negligible in the remainder of the domain).

4.5. Comparison with other idealized studies

This duality in the mechanisms leading to slantwise circulations was also found in the idealized dry two-dimensional numerical-model simulations of Morcrette and Browning (2006). They found that small regions of symmetric instability formed below the ΔM-adjustment updraught, and that a second updraught formed in the region where this instability was being released. They speculate that symmetric instability is also forming in the ΔM-adjustment region but that it is being removed by the upright convection and ΔM-adjustment process in such a way that large regions of instability cannot be diagnosed. This is consistent with the isolated regions found to satisfy the RSI diagnostic here in the main slantwise-ascending band (see, for example, Figures 4 and 11 (lower panels)). As noted by Morcrette and Browning (2006), the ΔM-adjustment process as described by Holt and Thorpe (1991) or Fischer and Lalaurette (1995b) cannot explain the low-level circulation.

These results differ from those found in other idealized modelling studies. Knight and Hobbs (1988) simulated a cold front forced by shear deformation in a moist two-dimensional primitive-equation model. A region of negative equivalent PV is lifted by the ageostrophic frontal circulation, and is associated with the development of a slanting (wide cold-frontal) rain band extending towards the cold air. Further rain bands form through convergence behind the rearmost rain band (that furthest from the region of line convection), and intensify as they move into the region of negative equivalent PV (in simulations with sufficient resolution). This development is similar to the three-stage process of frontal rain-band development suggested by Bennetts and Hoskins (1979) and referred to by Xu (1986a) as 'downscale development of CSI', except that Knight and Hobbs attribute the initial formation of the additional rain bands to mid-level convergence, whereas Bennetts and Hoskins attribute their formation to the release of conditional gravitational instability generated by the release of CSI. In our simulations, we attribute the formation of the main slantwise band to the release of inertial instability. Knight and Hobbs (1986) find positive absolute vorticity in the region of their bands, and attribute the formation of the main slantwise band to the release of CSI. We also find additional convection occurring in the cold air, but find it to be forced by convergence in the boundary layer, rather than at mid-levels as in Knight and Hobbs (1988).

Xu (1986a, 1986b, 1989, 1992) has investigated the possible roles of CSI in the formation of frontal rain bands using linear and nonlinear theory, the Sawyer–Eliassen equation, and a semi-geostrophic model. He finds that the release of pure CSI can produce single or multiple rain bands, but that it is difficult to explain long-lasting rain bands using the theory (Xu, 1986a, 1986b). Two-dimensional case-study simulations by Fischer and Lalaurette (1995a) also yielded a small growth rate of the CSI perturbation, implying that interactions with frontal forcing may be expected. Single (but not multiple) bands can occur when frontal forcing is combined with small positive geostrophic MPV (Emanuel, 1985; Thorpe and Emanuel, 1985). Multiple bands can occur when geostrophic frontal forcing is combined with negative geostrophic MPV (for sufficiently widespread forcing, and MPV that is sufficiently negative but not so negative as to initiate the release of viscous CSI) (Xu, 1989). Xu (1992) shows that a feedback can occur between moist circulation bands and geostrophic forcing anomalies, through the generation of mesoscale geostrophic potential-vorticity anomalies. This leads to multiple fine moist banding when this feedback generates banded structure in the forcing and geostrophic potential-vorticity fields. Xu (1989, 1992) finds that slantwise banding occurs, with the bands sloping towards the cold air, and multiple bands occur on the warm side of the region of maximum geostrophic forcing and the primary (strongest) band. This pattern of banding relative to the primary band, attributed to CSI release, has also been found in two-dimensional primitive-equation-model case-study simulations with moderate (but not strong) frontal forcing (Fischer and Lalaurette, 1995b). In our simulations, multiple banding occurs on the cold side of the surface frontal region and the primary band. The surface frontal region is on the warm side of the region of maximum geostrophic forcing in the initial conditions (see Figure 2), so the multiple banding may be occurring on the warm side of the region of maximum

DOI: 10.1002/qj

geostrophic forcing, as in Xu (1989, 1992) (determination of the geostrophic winds is problematic – see Section 3). However, the location of the multiple bands relative to the primary band here suggests that the mechanism found by Xu (1989, 1992) is not acting in this case.

5. Conclusions

Experiments have been performed using an idealized version of an operational forecast model to determine the mechanisms of interaction of upright and slantwise convection in banded frontal clouds, and their dependence on the strength of the deformational forcing, the low-level baroclinicity and the model representation of convection. Two mechanisms of frontal banding are considered: the release of CSI, identified using a diagnostic based on the VRS diagnostic of Dixon *et al*. (2002); and ΔM adjustment due to the inertial adjustment of mid-tropospheric subgeostrophic momentum anomalies (identified using absolute vorticity). Convective triggering through forced ascent at the leading edge of travelling cold pools is also identified.

The use of an idealized version of a high-resolution operational model (with 4 km horizontal grid boxes) implies that the findings should be applicable to operational forecasts, and distinguishes this work from other studies of banded frontal clouds or circulations that have used much more simplified idealized models (e.g. Xu, 1989, 1992; Holt and Thorpe, 1991; Jones and Thorpe, 1992; Morcrette and Browning, 2006) or case studies with coarser resolution (e.g. Nicosia and Grumm, 1999; Mathur *et al*., 1999; Schultz and Knox, 2007; Wolfsberg *et al*., 1986).

Line convection is triggered along the front. Slantwise bands extend from the top of the line-convection elements into the cold air. These frontal bands are advected by the along-front flow, and so become oriented northeastwards, anticlockwise from the westerly thermal wind. This early slantwise banding is primarily attributed to ΔM adjustment. A second low-level band forms later in the simulations, and is attributed to the release of CSI. These findings are consistent with those of the idealized dry two-dimensional numerical-model simulations of Morcrette and Browning (2006). The gently-sloping, vertically-stacked circulations observed towards the end of the simulations also resemble those observed in the case upon which the initial conditions were loosely based (Browning *et al*., 2001, figure 7), although this does not necessarily imply that they have been generated by the same mechanisms. The lateral spreading of the cold pool generated by the line convection triggers further upright convection in the cold air. These plumes intersect the upper-level slantwise band, and the resulting ΔM adjustment is likely to enhance the band. This behaviour was also found in the two-dimensional cloud-resolving model simulations of Pizzamei *et al*. (2005). However, unlike in this study, those simulations showed no evidence of the release of CSI.

Enhanced deformational strain is found to lead to earlier onset of convection and more coherent line convection. A stronger cold pool is generated, but its speed is reduced relative to that seen in experiments with weaker deformational strain, because of inhibition by the strain field. Three precipitation bands exist for about 2–3 h in the experiment with the strongest deformation strain; the spatial structure of these bands is consistent with those typically seen observationally. Stronger cold pools and earlier convective onset are also found for increased low-level baroclinicity in the initial conditions. Enhanced low-level baroclinicity also leads to the generation of more inertial instability by line convection (for a given capping height of convection), a weak increase in CSI release, and consequently greater strength (and, potentially, horizontal extension) of the slantwise circulations formed by ΔM adjustment. If a stronger deformation-strain field leads to stronger low-level baroclinicity at the time of convective initiation, then stronger slantwise circulations should also be associated with stronger deformation-strain fields (though it has not been possible to prove this with the simulations analysed here).

These conclusions are based on experiments without a convective-parametrization scheme. Experiments using the standard or a modified scheme for this model demonstrate known problems with the use of this scheme at the awkward 4 km grid length used in these simulations. These findings highlight the difficulties in representing frontal convection and banding in operational high-resolution numerical weather-prediction models.

Acknowledgements

The authors thank the Met Office for the use of their Unified Model and for the advice and support in using the model provided by the Met Office Joint Centre for Mesoscale Meteorology at the University of Reading. We also gratefully acknowledge the use of diagnostic and plotting tools supported by Chang-Gui Wang via the National Centre for Atmospheric Science (NCAS). Finally we thank David Schultz and an anonymous reviewer for their constructive comments which have improved this manuscript. This work was funded by an NERC grant.

References

Bennetts DA, Hoskins BJ. 1979. Conditional symmetric instability – a possible explanation for frontal rainbands. *Q. J. R. Meteorol. Soc.* **105**: 945–962.

Bishop CH, Thorpe AJ. 1994a. Frontal wave stability during moist deformation frontogenesis. Part I: Linear wave dynamics. *J. Atmos. Sci.* **51**: 852–873.

Bishop CH, Thorpe AJ. 1994b. Frontal wave stability during moist deformation frontogenesis. Part II: The suppression of nonlinear wave development. *J. Atmos. Sci.* **51**: 874–888.

Browning KA, Chapman D, Dixon RS. 2001. Stacked slantwise convective circulations. *Q. J. R. Meteorol. Soc.* **127**: 2513–2536.

Bukovsky MS, Kain JS, Baldwin ME. 2006. Bowing convective systems in a popular operational model: Are they for real? *Weather and Forecasting* **21**: 307–324.

Chaboureau J-P, Thorpe AJ. 1999. Frontogenesis and the development of secondary wave cyclones in FASTEX. *Q. J. R. Meteorol. Soc.* **125**: 925–940.

Cullen MJP, Davies T, Mawson MH, James JA, Coulter SC, Malcolm A. 1997. 'An overview of numerical methods for the next generation UK NWP and Climate Model'. Pp 425–444 in *Numerical Methods in Atmospheric and Ocean Modelling*, the Andre J. Robert memorial volume, Lin CA, Laprise R, Ritchie H (eds). Canadian Meteorological and Oceanographic Society: Ottawa, Ontario, Canada.

Dacre HF, Gray SL. 2006. Life-cycle simulations of shallow frontal waves and the impact of deformation strain. *Q. J. R. Meteorol. Soc.* **132**: 2171–2190.

Dixon RS, Browning KA, Shutts GJ. 2002. The relation of moist symmetric instability and upper-level potential-vorticity anomalies to the observed evolution of cloud heads. *Q. J. R. Meteorol. Soc.* **128**: 839–859.

Done JM, Craig GC, Gray SL, Clark PA, Gray MEB. 2006. Mesoscale simulations of organised convection: Importance of convective equilibrium. *Q. J. R. Meteorol. Soc.* **132**: 737–756.

Droegemeier KK, Wilhelmson RB. 1985. Three-dimensional numerical modelling of convection produced by interacting thunderstorm outflow. Part I: Control simulation and low-Level moisture variations. *J. Atmos. Sci.* **42**: 2381–2403.

Durran DR, Klemp TB. 1982. On the effects of moisture on the Brunt–Väisälä frequency. *J. Atmos. Sci.* **39**: 2152–2158.

Emanuel KA. 1983. On assessing local conditional symmetric instability from atmosphere soundings. *Mon. Weather Rev.* **111**: 2016–2033.

Emanuel KA. 1985. Frontal circulations in the presence of small moist symmetric stability. *J. Atmos. Sci.* **42**: 1062–1071.

Fischer C, Lalaurette F. 1995a. Mesoscale-β-scale circulations in realistic fronts. I: Steady basic state. *Q. J. R. Meteorol. Soc.* **121**: 1255–1283.

Fisher C, Lalaurette F. 1995b. Meso-β-scale circulations in realistic fronts. II: Frontogenetically forced basic states. *Q. J. R. Meteorol. Soc.* **121**: 1285–1321.

Forbes RM. 2002. *Numerical Model Parametrization of Ice Microphysics and the Impact of Evaporative Cooling on Frontal Dynamics*. PhD thesis, Reading University.

Gray SL, Browning KA. 2006. Reply to comments by David M. Schultz on 'Cloud resolving model simulations of banded clouds' (October A, 2005, 131, 2617–2637). *Q. J. R. Meteorol. Soc.* **132**: 2097–2099.

Gregory D, Rowntree PR. 1990. A mass flux convection scheme with representation of cloud ensemble characteristics and stability-dependent closure. *Mon. Weather Rev.* **118**: 1483–1506.

Hobbs PV, Biswas KR. 1979. The cellular structure of narrow cold-frontal rainbands. *Q. J. R. Meteorol. Soc.* **105**: 723–727.

Holt MW, Thorpe AJ. 1991. Localised forcing of slantwise motion at fronts. *Q. J. R. Meteorol. Soc.* **117**: 943–963.

Jones SC, Thorpe AJ. 1992. The three-dimensional nature of symmetric instability. *Q. J. R. Meteorol. Soc.* **118**: 227–258.

James PK, Browning KA. 1979. Mesoscale structure of line convection at surface cold fronts. *Q. J. R. Meteorol. Soc.* **105**: 371–382.

Knight DJ, Hobbs PV. 1988. The mesoscale and microscale structure and organisation of clouds and precipitation in midlatitude cyclones Part XV: A numerical modeling study of frontogenesis and cold-frontal rainbands. *J. Atmos. Sci.* **45**: 915–930.

Knox JA. 2003. 'Inertial instability'. Pp 1004–1013 in *Encyclopaedia of the Atmospheric Sciences*, Holton JR, Pyle J, Curry JA (eds). Elsevier: New York.

Kuo Y, Bresch JF, Cheng M-D, Kain JS, Parsons DB, Tao W-K, Zhang D-L. 1997. Summary of a mini workshop on cumulus parameterization for mesoscale models. *Bull. Am. Meteorol. Soc.* **78**: 475–491.

Lagouvardos KW, Lemâitre Y, Scialom G. 1993. Dynamical structure of a wide cold-frontal cloudband observed during Fronts 87. *Q. J. R. Meteorol. Soc.* **119**: 1291–1319.

Lean HW, Clark PA. 2003. The effects of changing resolution on mesoscale modelling of line convection and slantwise circulations in FASTEX IOP16 *Q. J. R. Meteorol. Soc.* **129**: 2255–2278.

Lock AP, Brown AR, Bush MR, Martin GM, Smith RNB. 2000. A new boundary layer mixing scheme. Part 1: Scheme description and single-column model tests. *Mon. Weather Rev.* **128**: 3187–3199.

Mathur MB, Brill KF, Seman CJ. 1999. Evolution of slantwise vertical motions in NCEP's mesoscale eta model. *Mon. Weather Rev.* **127**: 5–25.

Morcrette CJ, Browning KA. 2006. Formation and release of symmetric instability following Delta-M adjustment. *Q. J. R. Meteorol. Soc.* **132**: 1073–1089.

Nicosia DJ, Grumm RH. 1999. Mesoscale band formation in three major Northeastern United States snowstorms. *Weather and Forecasting* **14**: 346–368.

Novak DR, Bosart LF, Keyser D, Waldstreicher JS. 2004. An observational study of cold season-banded precipitation in northeast US cyclones. *Weather and Forecasting* **19**: 993–1010.

Novak DR, Waldstreicher JS, Keyser D, Bosart LF. 2006. A forecast strategy for anticipating cold season mesoscale band formation within eastern US cyclones. *Weather and Forecasting* **21**: 3–23.

Patoux J, Hakim GJ, Brown RA. 2005. Diagnosis of frontal instabilities over the Southern Ocean. *Mon. Weather Rev.* **133**: 863–875.

Persson POG, Warner TT. 1993. Nonlinear hydrostatic conditional symmetric instability: Implications for numerical weather prediction. *Mon. Weather Rev.* **121**: 1821–1833.

Pizzamei M, Gray SL, Browning KA. 2005. Cloud resolving model simulations of banded clouds. *Q. J. R. Meteorol. Soc.* **131**: 2617–2637.

Renfrew IA, Thorpe AJ, Bishop CH. 1997. The role of the environmental flow in the development of secondary frontal cyclones. *Q. J. R. Meteorol. Soc.* **123**: 1653–1675.

Rivals H, Cammas J-P, Renfrew IA. 1998. Secondary cyclogenesis: The initiation phase of a frontal wave observed over the eastern Atlantic. *Q. J. R. Meteorol. Soc.* **124**: 243–267.

Roberts NM. 2003. 'The impact of a change to the use of the convection scheme to high resolution simulations of convective events (Stage 2 report from the storm scale numerical modelling projects)'. JCMM Internal Report 142 (Forecasting Research Technical Report 407). Available from http://www.metoffice.gov.uk/research/nwp/publications/papers/technical_reports/index.html.

Schultz DM. 2006. Comments on 'Cloud-resolving model simulations of multiply-banded frontal clouds' by M. Pizzamei, S. L. Gray and K. A. Browning (October A, 2005, 131, 2617–2637). *Q. J. R. Meteorol. Soc.* **132**: 2095–2096.

Schultz DM, Knox JA. 2007. Banded convection caused by frontogenesis in a conditionally, symmetrically and inertially unstable environment. *Mon. Weather Rev.* **135**: 2095–2110.

Schultz DM, Schumacher PN. 1999. The use and misuse of conditional symmetric instability. *Mon. Weather Rev.* **127**: 2709–2732; Corrigendum. *Mon. Weather Rev.* **128**: 1573.

Shutts GJ. 1990. SCAPE charts from numerical weather prediction model fields. *Mon. Weather Rev.* **118**: 2745–2751.

Smith RK, Reeder MJ. 1988. On the movement and low level structure of cold fronts. *Mon. Weather Rev.* **116**: 1927–1944.

Thorpe AJ, Emanuel KA. 1985. Frontogenesis in the presence of small stability to slantwise convection. *J. Atmos. Sci.* **42**: 1809–1824.

Wilson DR, Ballard SP. 1999. A microphysically based precipitation scheme for the UK Meteorological Office Unified Model. *Q. J. R. Meteorol. Soc.* **125**: 1607–1636.

Wolfsberg DG, Emanuel KA, Passarelli RE. 1986. Band formation in a New England storm. *Mon. Weather Rev.* **114**: 1552–1569.

Xu Q. 1986a. Conditional symmetric instability and mesoscale rainbands. *Q. J. R. Meteorol. Soc.* **112**: 315–334.

Xu Q. 1986b. Nonlinear circulations in a symmetrically unstable flow. *J. Atmos. Sci.* **43**: 494–498.

Xu Q. 1989. Frontal circulations in the presence of small viscous moist symmetric stability and weak forcing. *Q. J. R. Meteorol. Soc.* **115**: 1325–1353.

Xu Q. 1992. Formation and evolution of frontal rainbands and geostrophic potential vorticity anomalies. *J. Atmos. Sci.* **49**: 629–648.

Xu Q. 2004. Nearly symmetric and nearly baroclinic instabilities in the presence of diffusivity. Part 2. Mode structures and energetics. *J. Fluid Mech.* **500**: 283–312.

Xu Q, Clark HE. 1985. The nature of symmetric instability and its similarity to convective and inertial instability. *J. Atmos. Sci.* **42**: 2880–2883.

DOI: 10.1002/qj